

# Graphene-Mercury-Graphene Sandwich Electrode for Electroanalysis

Tobias Grosser, Michel Wehrhold, Tilmann J. Neubert, and Kannan Balasubramanian\*<sup>[a]</sup>

We present a new class of hybrid 2D electrodes, where mercury is incorporated between two graphene monolayers, prepared by bottom-up assembly. First, the bottom graphene layer is electrochemically modified leading to the creation of fine mercury nanodroplets of variable size on the graphene surface. Although such electrodes show good sensitivity to heavy metal ions, their stability is limited due to the outgassing of mercury over time. After coverage with a top monolayer, the graphene surface is rendered with the favorable properties of mercury

such as the high overpotential for hydrogen evolution, the ability to work at a broader cathodic potential range and higher sensitivity towards heavy metal ions such as  $\text{Cd}^{2+}$  and  $\text{Pb}^{2+}$ . Most importantly, the outgassing of mercury is completely hindered by the top layer, which yields a stable mercury-like electrode but with a carbonaceous non-toxic interface. We attribute the favorable properties of the sandwich electrode to the subsurface mercury present below the top graphene sheet, which renders it with new electrochemical properties.


## Introduction


Carbon-based electrodes have attracted a lot of interest due to their favorable chemical and physical properties like high chemical resistance, high stability, and cost-effectiveness in comparison to metal electrodes.<sup>[1]</sup> Among them, graphene, as a versatile atomically thin electrode material, is a unique candidate, whose electrochemical properties at a single sheet level have been investigated in detail.<sup>[2]</sup> In contrast to metal electrodes, the electrochemistry at graphene monolayers is found to be sensitive to the preparation procedure, interfacial surface charge and to the occurrence of defects and edges,<sup>[3]</sup> which is reflected in the broad range of electron transfer rates reported.<sup>[4]</sup> When free of metallic trace impurities, they can have a broadly accessible potential range, without any parasitic signals from surface adsorption or oxidation processes typically observed on metal electrodes.<sup>[5]</sup> However, the potential range on the cathodic side is limited due to oxygen reduction and hydrogen evolution reactions at the carbon surface. Chemical modification of graphene is being widely pursued to modify the electrochemical characteristics.<sup>[3a,6]</sup> For example, deposition of metal nanoparticles may impart improved electrocatalytic activity in carbon electrodes.<sup>[7]</sup> Modification of an individual graphene monolayer with mercury and the ensuing effect on the electrochemical properties have not been reported yet.

Classically, mercury drop electrodes have long been used for applications in electroanalysis. In order to overcome toxicity issues<sup>[8]</sup> related to the use of elemental mercury in large amounts, mercury film electrodes have been deployed.<sup>[9]</sup> Carbon-based electrodes are well suited as supports to realize such films, as they allow preserving the unique electrochemical characteristics of mercury, such as the high overpotential for hydrogen evolution. This has enabled the detection of low amounts of heavy metal ions with applications e.g. in environmental analysis.<sup>[9b,10]</sup> Despite the comparative reduction in toxicity at mercury film electrodes, the presence of mercury microdroplets<sup>[11]</sup> open to the environment harbors the risk of outgassing, which may be harmful in larger amounts.<sup>[8a,12]</sup> While coalescence of mercury drops on electrode surfaces during growth has been reported,<sup>[13]</sup> the fate of mercury microdroplets after deposition has not received much attention. In some applications, the mercury film is formed in situ during electroanalysis to avoid such stability problems.<sup>[14]</sup> This approach bears the disadvantage that the mercury salt needs to be added during the sensor trials. From an application perspective, electrodes comprised of composites of graphene and mercury have been demonstrated.<sup>[14]</sup> However, there is no report yet of a standalone graphene bilayer electrode sandwiched with mercury.

In this work, we first present the modification of individual graphene monolayers with mercury, resulting in the formation of nanosized droplets. With the help of Atomic Force Microscopy (AFM) measurements, we follow the evolution of the droplets over time, which provide clear evidence for the outgassing of mercury under ambient conditions in air. The realized electrodes show favorable electrochemical properties as characterized using two model reactions: the electroanalysis of trace amounts of cadmium and lead ions and high overpotential for the hydrogen evolution reaction (HER). Subsequently, by covering the mercury droplets with a second graphene layer, we realize a bilayer graphene electrode sandwiched with mercury, where the outgassing of mercury is

[a] T. Grosser, M. Wehrhold, T. J. Neubert, Prof. Dr. K. Balasubramanian  
Department of Chemistry  
School of Analytical Sciences Adlershof (SALSA) & IRIS Adlershof  
Humboldt-Universität zu Berlin  
Unter den Linden 6, 10117 Berlin, Germany  
E-mail: nano.anchem@hu-berlin.de

 Supporting information for this article is available on the WWW under <https://doi.org/10.1002/celc.202101290>

 © 2021 The Authors. ChemElectroChem published by Wiley-VCH GmbH. This is an open access article under the terms of the Creative Commons Attribution Non-Commercial NoDerivs License, which permits use and distribution in any medium, provided the original work is properly cited, the use is non-commercial and no modifications or adaptations are made.

completely hindered. Moreover, at these hybrid electrodes the sensitivity towards heavy metal ions is largely preserved, with only a slight lowering of the accessible range of the cathodic potential.

## Results and Discussion

Monolayer graphene electrodes on Si/SiO<sub>2</sub> substrates with pre-patterned metal contacts were prepared as outlined in our earlier works.<sup>[3a,d]</sup> (see Figure S1 in supporting information (SI) and experimental section for details). In such devices, a single sheet of CVD-grown graphene is exclusively in contact with the electrolyte solution and serves as the working electrode. Mercury is electrodeposited on such electrodes potentiostatically from a nitrate solution. Figure 1 shows AFM images of unmodified graphene and graphene modified with mercury for two different deposition times. It is apparent that nanodroplets with varying sizes are formed on the graphene surface. The height profiles indicate particles of around 100 nm height for the shorter deposition time (Figure 1(b)). For long deposition times, large clusters are observed as shown in Figure 1(c). The size and density of the obtained droplets vary as we move away from the graphene edge region (see Figure S2 in SI for AFM images from the center of the graphene sheet). Since the graphene sheet is in contact with the metal lead only at one periphery, it is expected that there will be a variation of droplet density over the entire graphene sheet due to differences in the diffusion profile, the local electrochemical activity and the occurrence of defects.<sup>[3b,11b,15]</sup>

Proof that the deposited droplets are composed of mercury is obtained from Energy-Dispersive X-ray Spectroscopy (EDX). Figure 2(a) shows a Scanning Electron Microscopy (SEM) image of the peripheral region of a graphene sheet modified with Hg nanodroplets (Gr/HgND), where a high density of mercury droplets is visible. Figure 2(b) compares the EDX spectrum obtained on a droplet to that obtained on an unmodified graphene region, from where it is apparent that the droplet contains mercury. The droplets are found exclusively on the graphene sheet as attested by the map of the EDX Hg–M-line intensity in Figure 2(c), where no signal is discernible on the Si/SiO<sub>2</sub> substrate (for an EDX-map of the silicon line see Figure S3 in SI). On other carbon-based electrodes, electrodeposited mercury formed droplets with diameter in the micron range.<sup>[11]</sup> The nanodroplet form of mercury on the graphene surface may be due to several reasons. First, for electrodeposition, we have used a rather cathodic potential of  $-0.7$  V vs. Ag/AgCl, where the formation of smaller mercury droplets is favored.<sup>[11b]</sup> Secondly, electrodeposition by reduction of a metal salt typically results in small nanoparticles on a graphene surface, attributed often to locations of high electrochemical activity.<sup>[4,16]</sup> Finally, there might be a balance between surface tension and cohesive forces of the mercury droplet and the interaction with the graphene surface, resulting in the formation of such nanodroplets.<sup>[12]</sup>

The main advantages of mercury as an electrode material are the high overpotential for hydrogen evolution providing a

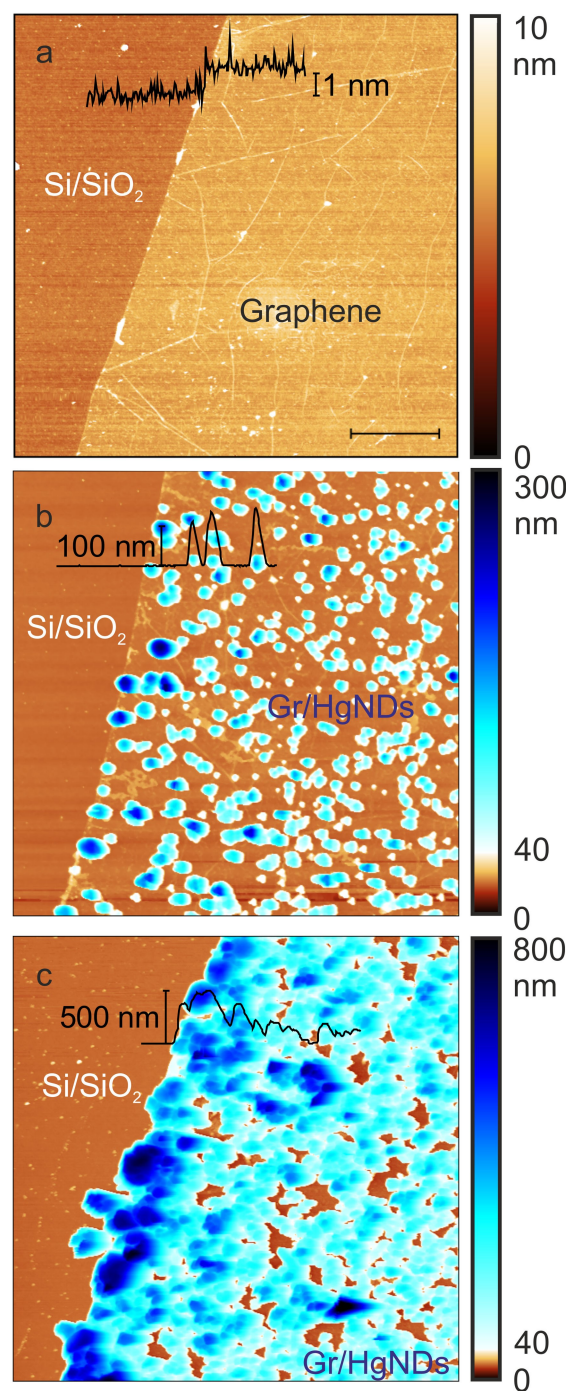


**Figure 1.** Atomic Force Microscopy (AFM) images of a graphene sheet on Si/SiO<sub>2</sub> before (a) and after coating (b, c) with mercury nanodroplets. In (b), the graphene/mercury nanodroplet (Gr/HgNDs) electrode was prepared by electrodeposition of mercury from a nitrate solution for 10 s, while in (c), the duration was 60 s. Lateral scale bar: 2  $\mu$ m.

large cathodic window and the high sensitivity for the detection of heavy metal ions such as cadmium and lead. However, on the anodic side, the usable potential range is rather limited. First, we will discuss the sensitivity of our electrodes towards the detection of heavy metal ions and subsequently discuss the

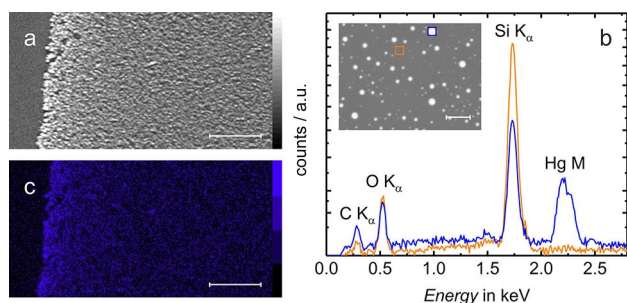


**Figure 2.** (a) Scanning Electron Microscopy (SEM) image of the peripheral region of a mercury modified graphene sheet on a Si/SiO<sub>2</sub> substrate, where a deposition time of 600 s was used. (left part of the image: Si/SiO<sub>2</sub>, right part: Hg-modified graphene). (b) Energy dispersive X-ray (EDX) spectra obtained on a Hg nanodroplet (blue curve) and on a graphene region without Hg (orange curve). The inset shows the location of the central region of the electrode, where the spectra were taken. (c) Map showing the intensity of the Hg–M line for the same region as in (a). Scale bar: 20 μm in (a) and (c), 2 μm in (b).

general electrochemical behavior in acidic solution. Square Wave Anodic Stripping Voltammetry (SWASV) was used to evaluate the detection capability of the realized electrodes towards cadmium ions. The electrode was held at a potential of  $-1.0$  V for 5 minutes in a buffered chloride solution of the heavy metal, followed by stripping of the deposited metal by sweeping the potential anodically. Figure 3(a) presents typical SWASV curves obtained at unmodified (Gr) and mercury-modified graphene (Gr/HgND) electrodes for two different concentrations of the metal salt. On unmodified graphene (black dashed curve), we do not see a response for cadmium ions at 100 nM, while a clear response can be observed for this concentration at the Gr/HgND electrode (blue dashed curve). The cathodic peak at  $-0.57$  V for the latter electrode (blue curves) is attributed to dissolved oxygen, whose current magnitude remains rather constant for all cadmium-ion concentrations. In order to obtain a calibration curve, we integrate the area below the peaks around the peak potential. A typical example of such a calibration curve for the two types of electrodes is shown in Figure 3(b), where it is apparent that the sensitivity is more than an order of magnitude higher at the Gr/HgND electrode than at the unmodified electrode. Moreover, we extract a detection limit of 50 nM (around 5 μg/L Cd<sup>2+</sup>), which is at least an order of magnitude lower at the Gr/HgND electrode. Hence, the Gr/HgND electrodes provide significant improvement in sensing performance. However, it should be noted that a direct comparison has some shortcomings, because the geometric and electrochemical areas for both types of electrodes are different and hence it is difficult to estimate a current density, which would be a better measure for comparison. On the other hand, the sensitivity and detection limit were close to the values shown in Figure 3 for several electrodes that we fabricated.

Now, we turn towards the realization of a graphene-mercury-graphene sandwich electrode, for which we cover the mercury-modified graphene electrode with a second layer of graphene. The motivation behind this is two-fold. First, there is evidence that graphene assumes the electrochemical and

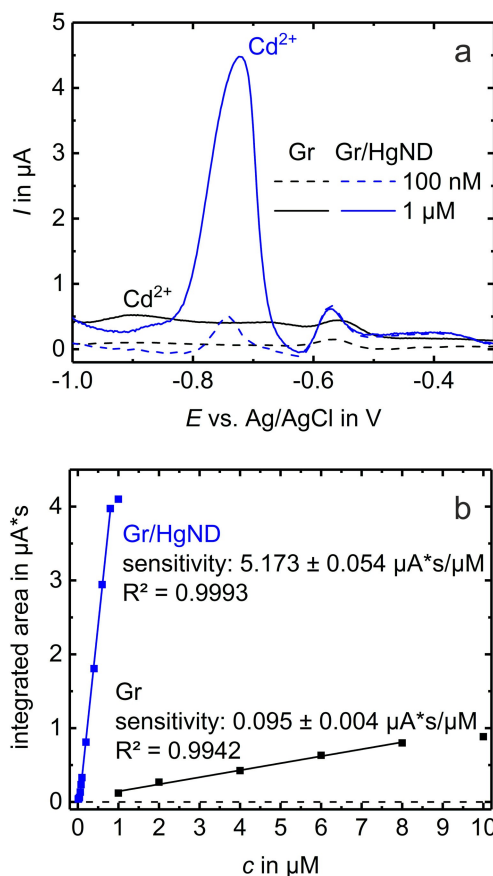


**Figure 3.** (a) Baseline-subtracted Square Wave Anodic Stripping Voltammetry (SWASV) data for the detection of Cd<sup>2+</sup> at a mercury-modified graphene electrode (Gr/HgND, blue curves), compared to that at a bare graphene electrode (Gr, black curves). (b) Calibration curves for Cd<sup>2+</sup> detection at a Gr and a Gr/HgND electrode, where the integrated area below the main peak in (a) is plotted as a function of analyte concentration. The square wave parameters were frequency: 50 Hz, pulse amplitude: 15 mV, potential step: 2 mV; acetate buffer pH 4.5. The fit was done for the concentration range, where the response was linear.

electrocatalytic properties of the underlying metal, mostly due to its single-atomic layer thickness.<sup>[17]</sup> While this has been shown with some metals like gold, there is no investigation yet on the effect of sub-surface mercury on the electrochemical properties of graphene. Secondly, we expect to reduce the outgassing of mercury using the second graphene layer. In the Gr/HgND electrodes discussed above, the amount of mercury ( $\sim 150$  ng/mm<sup>2</sup>) is drastically low in comparison to classical mercury drop and film electrodes. This is partly due to the formation of nanodroplets without the creation of a continuous film. The transfer of the second layer onto the Gr/HgND electrode can be followed at every step using optical microscopy (see Figures S4 and S5 in SI), which helps us to confirm the presence of an intact second layer. Figure 4 shows AFM images of a region of the sandwich electrode, where the second layer is partly covering the first layer. Such a sample was prepared mainly to characterize the morphology of the trapped droplets. Usually, we prepare a second layer in such a way that it covers the first layer almost completely. In the amplitude



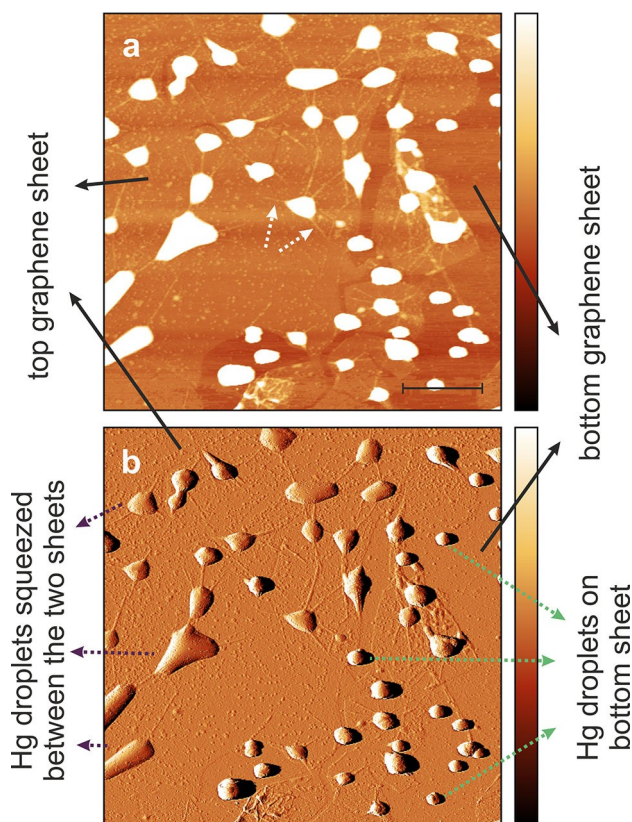


**Figure 4.** Simultaneously acquired AFM height (a) and amplitude (b) images of a sandwich electrode (Gr/HgND/Gr). Both AFM images show the same region, where the first layer with mercury nanodroplets is mostly covered with the second graphene sheet on top. On the first layer, the mercury droplets appear as hemispherical balls. The trapped mercury droplets (indicated by the purple dashed arrows in (b)) are not hemispherical and appear squeezed due to the top layer. The white dashed arrows in (a) indicate folds appearing on the top layer due to the presence of the underlying droplets. (lateral scale bar: 2  $\mu\text{m}$ , color scale: 57 nm for (a) and 0.18 V for (b)).

image (Figure 4(b)), we can distinguish the droplets present on the first layer from those that are trapped between the two layers. The droplets on the first layer (some of them are indicated by the green dotted arrows in Figure 4(b)) are mostly spherical, while the droplets trapped between the two layers (indicated using purple dashed arrows in Figure 4(b)) appear squeezed due to the presence of the top graphene sheet. Furthermore, characteristic line folds appear around the trapped and squeezed droplets (marked by the white dashed arrows in Figure 4(a)), which we attribute to stress developing on the top layer due to the underlying spike-like nanodroplets. This is comparable to folds appearing when a blanket is placed over an array of stones.

We have also performed confocal Raman spectroscopy to assess the effect of mercury on the graphene layers and to confirm the presence of intact graphene layers. Typical Raman spectra obtained at the various stages of the fabrication are shown in Figure 5. The Raman spectrum after the first transfer (black curve) shows clear G and 2D peaks confirming the presence of a graphene monolayer.<sup>[18]</sup> The intensity of the 2D-peak ( $I_{2D}$ ) is higher than the G-peak intensity ( $I_G$ ), which is

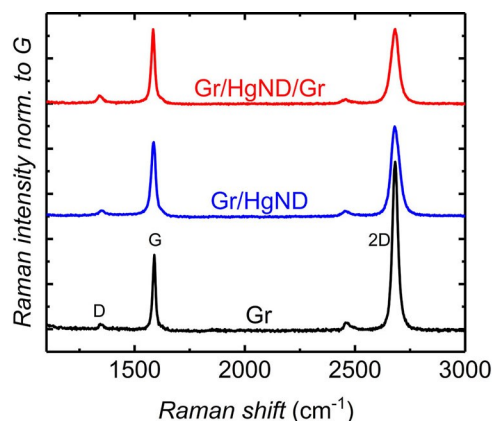


**Figure 5.** Raman spectra obtained during the various stages of the preparation of the sandwich electrode. Excitation wavelength: 532 nm. The Raman intensities are normalized to the intensity of the G-peak.

typically observed in our graphene samples on  $\text{SiO}_2$ . The D-peak intensity ( $I_D$ ) is low, indicative of graphene with low defects or disorder. The blue curve was obtained on a mercury nanodroplet after deposition on the first graphene layer. It is apparent that the  $I_{2D}/I_G$  ratio decreases, which can be explained by charge carrier doping due to mercury.<sup>[19]</sup> In the Raman spectrum obtained after the transfer of the second graphene layer (red curve), again the typical graphene bands are visible, confirming the presence of the second layer. The  $I_{2D}/I_G$  goes down further, pointing towards some interaction between the mercury droplet and the top layer: These observations confirm the presence of the graphene sheet on top of the mercury nanodroplets in the sandwich electrode.

In order to study the temporal evolution of the mercury droplets on both types of electrodes, AFM was utilized again. Figures 6(a) and (b) present typical AFM images of a mercury-modified graphene sheet and a sandwich electrode respectively. Using such AFM images, we have tracked the stability of the same mercury droplets after deposition and after the transfer of second graphene layer in the two types of electrodes respectively over several days. For this purpose, we record AFM images of the same area and obtain a measure of the particle height as a function of time on both types of electrodes as shown in Figure 6(c). It is apparent that on Gr/HgND electrodes, where the nanodroplets are exposed to air, a clear reduction in particle height is seen over time. (Figure S6 in SI shows another example). This is also attested by the continued reduction in sensing performance over time (see Figure S7). By contrast, on the sandwich electrodes, the particle height remains rather unchanged even up to a duration of more than a week.

Next, we present the sensing performance of the sandwich electrode and evaluate if such electrodes are applicable for multiplex analysis. Figure 7(a) shows typical SWASV data obtained in a solution containing both  $\text{Cd}^{2+}$  and  $\text{Pb}^{2+}$  ions at a Gr/HgND electrode and at a sandwich electrode. It is apparent that both electrodes are amenable for multiplex analysis of heavy metal ions and that the currents at the sandwich electrode are only slightly lower than at the uncovered Gr/

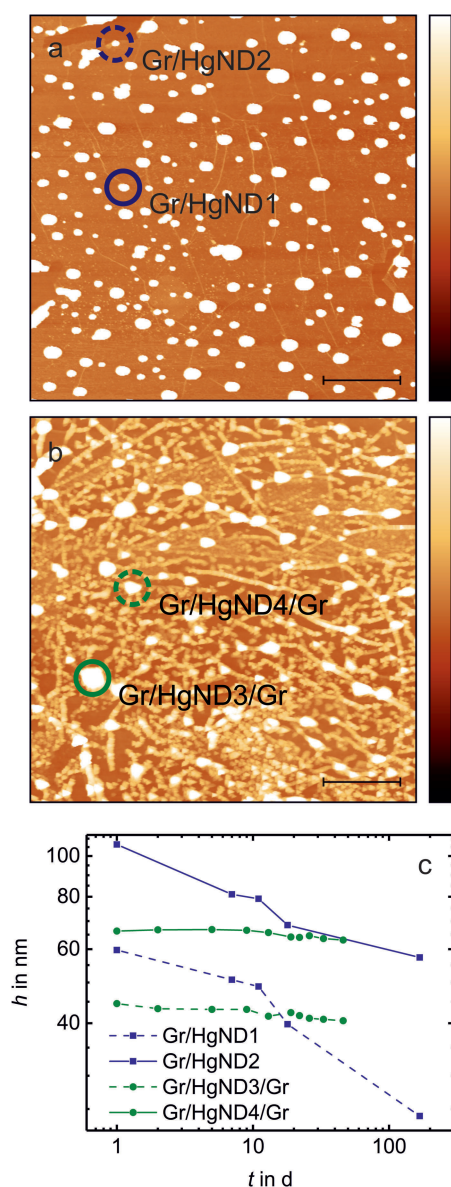


**Figure 6.** AFM images of (a) a mercury-modified graphene electrode Gr/HgND and (b) a sandwich electrode (Gr/HgND/Gr), the latter prepared by transferring a second graphene sheet onto a Gr/HgND electrode. (c) Evolution of particle height over time observed at two particle locations in each of the two devices. (lateral scale bar in a and b: 2  $\mu\text{m}$ , height scale: 40 nm). Another example is shown in Figure S6 in SI.

HgND electrodes. From the calibration curves for the detection of  $\text{Cd}^{2+}$  in Figure 7(b), we can conclude that the sensitivity is only slightly inferior after covering the electrode with the second graphene layer. Moreover, we obtain a similar detection limit at the sandwich electrode (Figure 7(c)) as at a freshly prepared uncovered Gr/HgND electrode. In any case, the sandwich electrode with a graphene interface shows clearly an improved performance in comparison to an unmodified monolayer graphene electrode.

Such a transfer of the favorable properties from mercury to the top graphene layer can be partly explained by the electronic coupling of mercury to the graphene monolayer.<sup>[17]</sup>

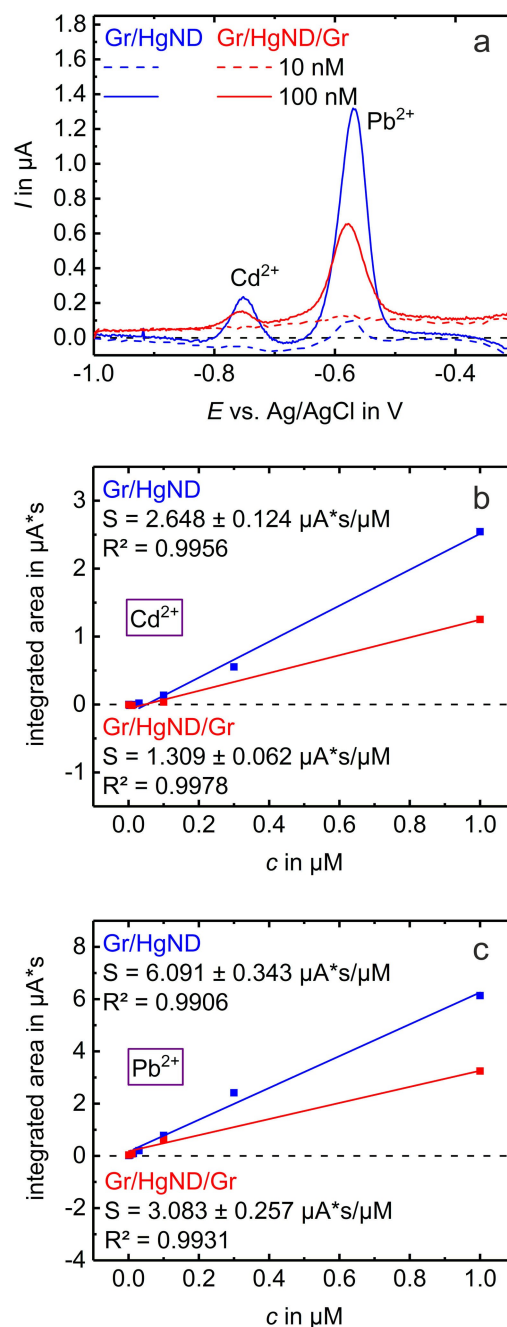


**Figure 7.** (a) Baseline-subtracted SWASV data showing multiplex detection of  $\text{Cd}^{2+}$  and  $\text{Pb}^{2+}$  at a mercury-modified graphene electrode (Gr/HgND) compared to the response at a sandwich electrode (Gr/HgND/Gr). The square wave parameters were: frequency 50 Hz, pulse amplitude 15 mV and potential step 2 mV; acetate buffer pH 4.5. (b, c) Comparison of calibration curves at the two different electrodes for the detection of  $\text{Cd}^{2+}$  and  $\text{Pb}^{2+}$  (within the linear concentration range), extracted from SWASV data, such as that in (a).  $S$ : sensitivity.

However, unlike in a mercury drop electrode, there is most likely no amalgam formation or dissolution of ions into mercury, since such a process is expected to be blocked by the top graphene layer. On the other hand, we have seen that bare graphene itself can be used as an electrode to pre-concentrate heavy metal ions by electroreduction. Hence, we suppose that

such a pathway is enhanced on the sandwich electrode through the underlying mercury nanodroplet, probably through the suppression of hydrogen evolution in this potential range. Since the dissolution during the stripping phase was very fast, we were not able to perform surface characterization of the electrodes after the pre-concentration step. Future in situ surface characterization experiments may help clarify the exact mechanism. In contrast to Gr/HgND electrodes (see Figure S8 in SI), the sensing performance of the sandwich electrodes remained rather unaffected even after three weeks (see Figure S9 in SI). The main resulting advantage is that such electrodes can be prepared well before use and hence do not require in situ electrodeposition of mercury during electroanalysis, thereby significantly simplifying the procedure for performing the sensing trials.

We have subsequently evaluated the applicability of our electrodes to the analysis of heavy metal ions in tap water. Figure 8(a) shows the typical sensor response of a Gr/HgND/Gr sandwich electrode to varying concentrations of cadmium ions spiked directly into tap water. Although the peaks are broader, a clear dependence of the sensor response to increasing concentration of  $\text{Cd}^{2+}$  is observed. We attribute the broadening

of the SWASV response to matrix effects, as we have directly used tap water without any pretreatment or ionic strength adjustment. Figure 8(b) presents the calibration curve extracted based on the integrated peak area, where a clear linear dependence of the sensor response to the heavy metal ion concentration is observable. The sensitivity and detection limit of the sandwich electrode in tap water are inferior to that observed in buffer solutions. Table S1 (in SI) compares the sensor performance of our electrodes with several other reports that have utilized carbon-based electrodes with electrodeposited mercury films. We can achieve a detection limit in the few  $\mu\text{g/L}$  range in buffer solutions similar to those of other electrodes. However, in contrast to the other electrodes, our procedure does not require the in situ deposition of mercury. Moreover, there is no outgassing or leakage of mercury, which provides significantly higher stability and safety than previously reported electrodes.

Finally, we discuss the effect of mercury incorporation on the hydrogen evolution characteristics and on the accessible anodic potential range. Figure 9 compares typical cyclic voltammograms (CVs) obtained at an unmodified graphene

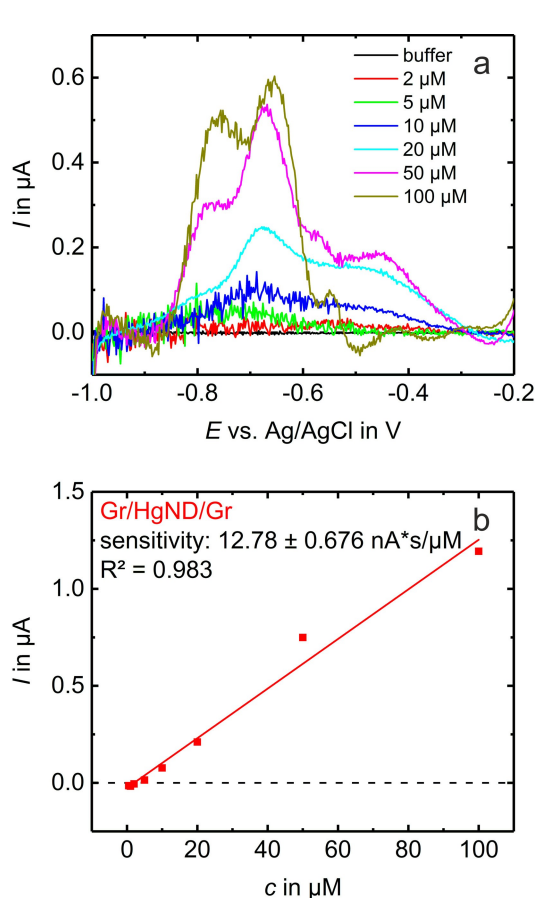


**Figure 8.** (a) Baseline-subtracted SWASV data measured at a sandwich electrode (Gr/HgND/Gr), showing the detection of varying concentrations of  $\text{Cd}^{2+}$ , directly spiked in tap water. The square wave parameters were: frequency 50 Hz, pulse amplitude 15 mV and potential step 2 mV. (b) Calibration curve for the detection of  $\text{Cd}^{2+}$  extracted from SWASV data in (a).

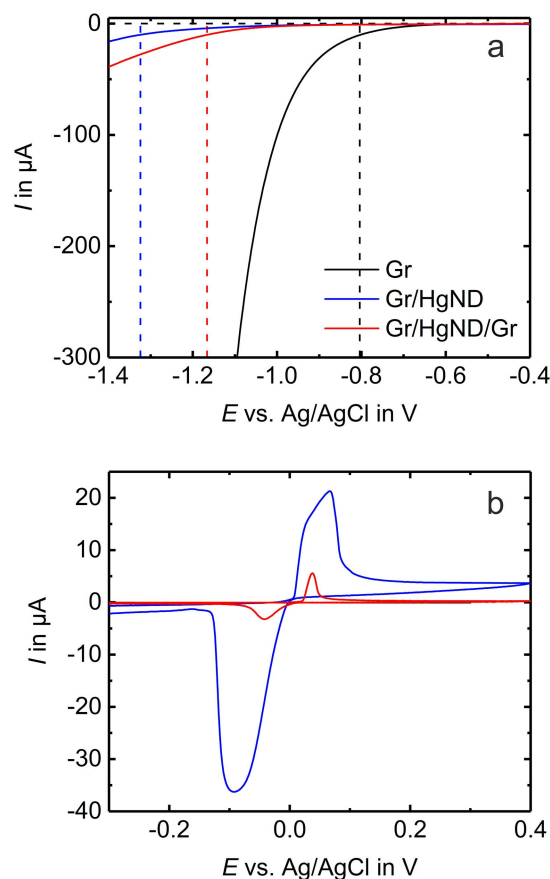


**Figure 9.** CVs measured at an unmodified graphene (Gr) electrode, at a mercury-modified graphene electrode (Gr/HgND) and at a sandwich electrode (Gr/HgND/Gr) in a nitrogen-saturated aqueous solution of 0.1 M HCl: (a) cathodic regime and (b) anodic regime. In (a) the dashed vertical lines give a rough qualitative idea of the onset potential for hydrogen evolution. In (b) the response for Gr is close to zero, and is hence not discernible in the graphs. Scan rate: 50 mV/s.



(Gr), at a mercury-modified graphene (Gr/HgND) and at a sandwich (Gr/HgND/Gr) electrode in acidic media saturated with nitrogen. On the cathodic side (Figure 9(a)), a sizeable current due to hydrogen evolution is observed at low overpotential on the Gr electrode similar to previous reports.<sup>[20]</sup> Among all three electrodes, the current due to hydrogen evolution is lowest at the Gr/HgND electrode. At the sandwich electrode, the magnitude of current due to hydrogen evolution is at an intermediate level between the Gr and Gr/HgND electrodes. Although the upper layer is graphene in a sandwich electrode, HER is hindered here due to the presence of underlying mercury. By contrast, for the first graphene layer, the underlying substrate is SiO<sub>2</sub>, where significant hydrogen evolution is expected. These observations are consistent with the expectation that the electrochemistry of graphene can be modulated by subsurface metal structures.<sup>[21]</sup> On graphitic electrodes with enriched edges, fast kinetics of HER has been reported.<sup>[22]</sup> By contrast, in our electrodes, edges constitute only a minuscule proportion of the electrode surface since the graphene sheet is mostly intact with just a few holes and cracks. Hence, the response in our electrodes is dominated mainly by the basal plane region. On the other hand, the presence of other kinds of defects (point defects, chemical modification) in the basal plane region cannot be excluded, where the HER may be catalyzed. In Gr/HgND and in sandwich electrodes, we believe that these defects are bridged through the presence of the mercury droplets (especially at high density), thereby slowing down the kinetics of HER. It is also worth mentioning that we perform only a few cycles of CV for measuring the hydrogen evolution response, in order to avoid damage to the graphene sheet that could be caused due to the evolution of hydrogen.<sup>[20b]</sup>

On the anodic side (Figure 9(b)), we see some redox peaks at the Gr/HgND electrode (blue curve), which we attribute to chloride formation and dissolution in the mercury nanodroplets.<sup>[23]</sup> Interestingly, by covering with a second graphene layer, this redox behavior is suppressed to a considerable extent, suggesting that most of the mercury droplets are covered by the second layer. It is worth mentioning that the typical size of the transferred graphene sheets is 2 × 2 mm and hence it is not possible to avoid small cracks or mechanical stress in the upper layer completely. On the other hand, chloride ions may still diffuse through the interstices between the two graphene sheets, which may be responsible for the observed redox peaks.<sup>[24]</sup> This is however unlikely for the heavy metal ions. Nevertheless, we have observed that these redox peaks could be further suppressed (however not completely) by transfer of a third graphene layer on top (see Figure S10 in SI).

## Conclusions

In conclusion, we have demonstrated the electrochemical decoration of single graphene sheets with mercury nanodroplets. The electrochemical characteristics of such electrodes resemble that of classical mercury film electrodes. However, we

have observed that mercury outgasses from such an electrode, providing poor stability. By covering these electrodes with a second graphene layer, we have shown a new class of sandwich electrodes, comprised of a bilayer with intercalated mercury nanodroplets. These electrodes are found to be stable and non-toxic, as we have shown that the outgassing of mercury is almost completely blocked. Furthermore, such electrodes provide information about the effect of subsurface mercury on the electrochemical characteristics of a single graphene sheet. Although the mercury droplets are covered, the sandwich electrodes exhibit higher overpotential for hydrogen evolution and an improved sensitivity for heavy metal ions, in comparison to an unmodified graphene electrode. We attribute this behavior to the synergistic effect between the electrochemical properties of graphene and mercury, with the special characteristic that the electrode interface is made up of carbon.

## Experimental Section

### Reagents

HCl (35%), H<sub>2</sub>O<sub>2</sub> (33%) and sulfuric acid (95%) were purchased from VWR, poly(styrene) (PS), lead(II) chloride and cadmium(II) chloride from Sigma-Aldrich, mercury(II) nitrate hydrate from Alfa Aesar, toluene and *N*-ethyl-2-pyrrolidone (NEP) from Roth, acetone and 2-propanol from BASF, glacial acetic acid from Fischer and sodium acetate from SERVA. All chemicals were used without further purification and solutions were prepared with ultra-pure water (Barnstead™ Easypure™ II, 18.2 MΩ cm).

### Instrumentation

The electrochemical measurements were performed in a 10 mL glass beaker using a 3-electrode setup comprising a Ag/AgCl electrode as reference, a platinum wire as counter electrode and (modified) graphene electrode on a Si/SiO<sub>2</sub> chip as the working electrode.

### Fabrication of Electrodes

Electrode lines with 50 nm Ti/10 nm Pt were structured on Si/SiO<sub>2</sub> substrates using standard photolithography and metal deposition. The substrates were cleaned successively with NEP, acetone, isopropanol and piranha solution (sulfuric acid: H<sub>2</sub>O<sub>2</sub>, 3:1), whereby sonication was used for the cleaning steps in NEP and acetone. 50 mg PS was dissolved in 1 mL toluene and the resulting solution was drop-cast onto CVD-grown graphene on copper foil (Graphenea). The foil was dried for 10 min at 75 °C and cut into rectangular pieces (a few mm<sup>2</sup> in size). A metal-ion free etching solution containing 1.8 M HCl and 0.5 M H<sub>2</sub>O<sub>2</sub> was used to remove the underlying copper. Afterwards, PS-coated graphene pieces were transferred onto Si/SiO<sub>2</sub> chips in such a way that graphene contacted the platinum leads. After drying the chips for 10 min at 95 °C, PS was washed away in toluene for about 3 minutes and the chips were dried again at 75 °C for 10 min. Next, the chips were annealed at 600 °C under nitrogen atmosphere for 2 minutes to remove organic traces, improve the adhesion between graphene and the substrate and increase the conductivity of graphene. Insulation of the electrode lines was achieved by spotting a solution of 800 mg/mL PS in toluene and then allowing to dry overnight. Finally, an electrochemical cleaning step<sup>[5]</sup> was used to remove

trace impurities such as copper on the graphene surface. This was performed in 100 mM HCl by using cyclic voltammetry with 20 cycles in a range from  $-0.6$  to  $+0.3$  V vs. Ag/AgCl.

Mercury-modified graphene (Gr/HgND) electrodes were prepared by deposition of mercury onto the graphene electrodes by applying a potential of  $-0.7$  V vs. Ag/AgCl in 10 mL solution of a 100  $\mu\text{g}/\text{mL}$  mercury(II) nitrate, which was acidified with 10 mM hydrochloric acid. In order to study the effect of deposition time, several samples with differing deposition times were prepared.

Sandwich electrodes (Gr/HgND/Gr) were made by transferring a second graphene sheet onto the Gr/HgND electrode. This was realized in the same way as the transfer of the first graphene sheet, without any previous cleaning of the Gr/HgND-chip. To avoid evaporation of the mercury, the electrodes were not dried in the oven, but instead left to dry overnight at room temperature. Afterwards, PS was washed away and the contacts were isolated with PS.

### Characterization

Scanning electron microscopy (SEM) images and energy dispersive X-ray spectroscopy (EDX) measurements were carried out with an JCM-6000 device from JEOL. The investigations were done under reduced pressure (low-vacuum mode of the device) to prevent mercury evaporation. The accelerating voltage was 15 keV and the back-scattered electron detector was used. Atomic force microscopy (AFM) images were obtained using a Nanoscope Dimension 3100 in tapping mode or a JPK Nanowizard 4 in AC imaging mode. Raman spectra were obtained on a JASCO NRS-4100 confocal Raman microscope using a  $1650 \times 256$  CCD detector (Andor, peltier-cooled  $-61^\circ\text{C}$ ), 900 lines/mm grating, laser excitation of 532 nm,  $100\times$  objective and a power of 5.6 mW. The spectra were acquired with an exposure time of 2 s and two accumulations.

### Sensing Trials

All electrochemical measurements for heavy metal detection were carried out in acetate buffer (pH = 4.5, 0.1 M). Square wave anodic stripping analysis was used as the electrochemical measurement method and a fresh sample was used for each measurement to prevent contamination of the electrode surface. Pre-cleaning of the surface was realized by applying a potential of  $-0.3$  V vs. Ag/AgCl for 60 s. After the cleaning step, the potential was switched to  $-1$  V vs. Ag/AgCl and held for 5 minutes for deposition of the heavy metals. A magnetic stirrer was used during the cleaning step and for 200 s of the deposition step to increase the amount of the electrodeposited heavy metal. During the last 100 s of the deposition step, stirring was stopped to avoid turbulences during the subsequent stripping step. Square wave voltammetry was chosen, where a frequency of 50 Hz, a pulse amplitude of 15 mV and a potential step of 2 mV was used. The determination of the hydrogen evolution onset was carried out in a deoxygenated 100 mM HCl solution. Deoxygenation was realized by bubbling the solution for 5 minutes with nitrogen gas. For measuring the sensor response in tap water, first the background response was measured using SWASV directly in tap water. Following this, the response to increasing concentrations of heavy metal ions was measured by spiking an appropriate amount of a concentrated stock solution to the tap water sample.

### Safety Measures

Although working with an amount of less than 1  $\mu\text{g}$  mercury per chip, necessary precautions were taken to ensure safe working with

chemicals involving mercury. All measurements were done in a fume hood. Only for AFM and SEM experiments, the samples were taken and placed into the AFM or SEM enclosure. The enclosures were ventilated after use.

### Acknowledgements

Funding from the German Science Foundation (DFG) via the Graduate School of Analytical Sciences Adlershof (SALSA GSC1013) and via INST 276/754-1 is acknowledged. We acknowledge Stephan Schmid and Birgit Lemke of MPI Stuttgart, Martin Muske of HZB and Michael Winterfeld of HU Berlin for help with metal deposition, wafer cutting, lithography and AFM measurements. We thank Anur Yadav for discussions. Open Access funding enabled and organized by Projekt DEAL.

### Conflict of Interest

The authors declare no conflict of interest.

**Keywords:** 2D materials · graphene · intercalations · electrochemical modification · mercury film

- [1] a) E. Frackowiak, F. Beguin, *Carbon* **2001**, *39*, 937–950; b) G. Henze, in *Polarographie und Voltammetrie: Grundlagen und analytische Praxis*, Springer Berlin Heidelberg, Berlin, Heidelberg, **2001**, pp. 66–100; c) B. Uslu, S. A. Ozkan, *Anal. Lett.* **2007**, *40*, 817–853; d) S. A. Wring, J. P. Hart, *Analyst* **1992**, *117*, 1215–1229.
- [2] a) D. A. C. Brownson, D. K. Kampouris, C. E. Banks, *Chem. Soc. Rev.* **2012**, *41*, 6944–6976; b) W. Li, C. Tan, M. A. Lowe, H. D. Abruña, D. C. Ralph, *ACS Nano* **2011**, *5*, 2264–2270; c) N. L. Ritzert, J. Rodríguez-López, C. Tan, H. D. Abruña, *Langmuir* **2013**, *29*, 1683–1694; d) A. T. Valota, P. S. Toth, Y.-J. Kim, B. H. Hong, I. A. Kinloch, K. S. Novoselov, E. W. Hill, R. A. W. Dryfe, *Electrochim. Acta* **2013**, *110*, 9–15.
- [3] a) A. Yadav, M. Wehrhold, T. J. Neubert, R. M. Iost, K. Balasubramanian, *ACS Appl. Nano Mater.* **2020**, *3*, 11725–11735; b) J.-H. Zhong, J. Zhang, X. Jin, J.-Y. Liu, Q. Li, M.-H. Li, W. Cai, D.-Y. Wu, D. Zhan, B. Ren, *J. Am. Chem. Soc.* **2014**, *136*, 16609–16617; c) A. G. Güell, N. Ebejer, M. E. Snowden, J. V. Macpherson, P. R. Unwin, *J. Am. Chem. Soc.* **2012**, *134*, 7258–7261; d) M. Wehrhold, T. J. Neubert, A. Yadav, M. Vondráček, R. M. Iost, J. Honolka, K. Balasubramanian, *Nanoscale* **2019**, *11*, 14742–14756.
- [4] L. J. A. Macedo, R. M. Iost, A. Hassan, K. Balasubramanian, F. N. Crespilho, *ChemElectroChem* **2019**, *6*, 31–59.
- [5] R. M. Iost, F. N. Crespilho, L. Zuccaro, H. K. Yu, A. M. Wodtke, K. Kern, K. Balasubramanian, *ChemElectroChem* **2014**, *1*, 2070–2074.
- [6] G. Bottari, M. Á. Herranz, L. Wibmer, M. Volland, L. Rodríguez-Pérez, D. M. Guldi, A. Hirsch, N. Martín, F. D'Souza, T. Torres, *Chem. Soc. Rev.* **2017**, *46*, 4464–4500.
- [7] D. Hernández-Santos, M. B. González-García, A. C. García, *Electroanalysis* **2002**, *14*, 1225–1235.
- [8] a) R. A. Bernhoft, *J. Environ. Health* **2012**, *2012*, 460508–460508; b) J. Mercola, D. Klinghardt, *J. Nutr. Environ. Med.* **2001**, *11*, 53–62.
- [9] a) A. Economou, P. R. Fielden, *Analyst* **2003**, *128*, 205–213; b) V. Vyskočil, J. Barek, *Crit. Rev. Anal. Chem.* **2009**, *39*, 173–188.
- [10] G. March, T. D. Nguyen, B. Piro, *Biosensors* **2015**, *5*.
- [11] a) J. Wang, B. Tian, *Anal. Chem.* **1992**, *64*, 1706–1709; b) M. Štulíková, *J. Electroanal. Chem. Interfacial Electrochem.* **1973**, *48*, 33–45.
- [12] A. E. Galashev, V. A. Polukhin, *Russ. J. Phys. Chem. A* **2015**, *89*, 1429–1433.
- [13] C. Liu, W. Cheng, Q. Zeng, X. Huang, L. Wang, *J. Electroanal. Chem.* **2017**, *784*, 145–152.
- [14] S. Zbeda, K. Pokpas, S. J. Titinchi, N. Jahed, P. Baker, E. I. Iwuoha, *Int. J. Electrochem. Sci.* **2013**, *8*, 11125–11141.



- [15] L. J. A. Macedo, F. C. D. A. Lima, R. G. Amorim, R. O. Freitas, A. Yadav, R. M. Iost, K. Balasubramanian, F. N. Crespilho, *Nanoscale* **2018**, *10*, 15048–15057.
- [16] K. Balasubramanian, L. Zuccaro, K. Kern, *Adv. Funct. Mater.* **2014**, *24*, 6348–6358.
- [17] J. Hui, X. Zhou, R. Bhargava, A. Chinderle, J. Zhang, J. Rodríguez-López, *Electrochim. Acta* **2016**, *211*, 1016–1023.
- [18] A. C. Ferrari, J. C. Meyer, V. Scardaci, C. Casiraghi, M. Lazzeri, F. Mauri, S. Piscanec, D. Jiang, K. S. Novoselov, S. Roth, A. K. Geim, *Phys. Rev. Lett.* **2006**, *97*, 187401.
- [19] a) D. M. Basko, S. Piscanec, A. C. Ferrari, *Phys. Rev. B* **2009**, *80*, 165413; b) A. Das, S. Pisana, B. Chakraborty, S. Piscanec, S. K. Saha, U. V. Waghmare, K. S. Novoselov, H. R. Krishnamurthy, A. K. Geim, A. C. Ferrari, A. K. Sood, *Nat. Nanotechnol.* **2008**, *3*, 210–215.
- [20] a) A. Xie, N. Xuan, K. Ba, Z. Sun, *ACS Appl. Mater. Interfaces* **2017**, *9*, 4643–4648; b) A. García-Miranda Ferrari, D. A. C. Brownson, C. E. Banks, *Sci. Rep.* **2019**, *9*, 15961.
- [21] J. Hui, S. Pakhira, R. Bhargava, Z. J. Barton, X. Zhou, A. J. Chinderle, J. L. Mendoza-Cortes, J. Rodríguez-López, *ACS Nano* **2018**, *12*, 2980–2990.
- [22] M. P. J. Brennan, O. R. Brown, *J. Appl. Electrochem.* **1972**, *2*, 43–49.
- [23] M. A. Nolan, S. P. Kounaves, *Electroanalysis* **2000**, *12*, 96–99.
- [24] S. Wang, C. Wang, X. Ji, *RSC Adv.* **2017**, *7*, 52252–52260.

Manuscript received: September 21, 2021

Accepted manuscript online: October 26, 2021